Journal of Materials Chemistry C

ROYAL SOCIETY OF CHEMISTRY

PAPER

View Article Online
View Journal | View Issue

Cite this: J. Mater. Chem. C, 2024, 12, 5496

[001]-Oriented heteroepitaxy for fabricating emissive surface mounted metal–organic frameworks†

Tonghan Zhao, *[a] Narges Taghizade, [b] Jan C. Fischer,[a] Bryce S. Richards [ac] and Ian A. Howard ‡*[ac]

Received 2nd January 2024,
Accepted 16th March 2024

DOI: 10.1039/d4tc00018h

rsc.li/materials-c

Well-oriented growth of surface-anchored metal–organic frameworks (SURMOFs) makes them ideal candidates for optical sensor applications. In this work, SURMOF bilayers and trilayers that exhibit [001] orientation are formed *via* heteroepitaxial growth. Using liquid-phase epitaxy (LPE), a ⟨100⟩ silicon substrate is alternatingly exposed to a solution of metal salts and organic linkers. A $Cu_2(BDC)_2(DABCO)$ basis layer allows subsequent deposition of $Zn_2(BDC)_2(DABCO)$ with 93% of the material aligned in the crystallographic [001] orientation. This is not possible without a Cu-SURMOF seed layer. Out-of-plane X-ray diffraction, 2D grazing-incidence wide-angle X-ray scattering, and scanning electronic microscopy techniques reveal that the hybrid SURMOFs display oriented island-type film growth, resulting in multi-shell islands. A third oriented SURMOF $Zn_2(ADC)_2(BPy)$ can be added to endow the heterostructure with photoluminescence, which is not quenched by the Cu-SURMOF due to the intermediate $Zn_2(BDC)_2$-(DABCO) layer. Conceptually, the step-by-step LPE deposition method allows the construction of monolithic multilayer SURMOFs wherein the orientation can be controlled by well-behaved templating layers and functionality can be added by more exotic layers that are challenging to grow on their own.

Introduction

Metal–organic frameworks (MOFs) – built from inorganic ions/clusters and organic ligands – are ideal candidates for optical sensing,[1,2] information encryption,[3] and bioimaging,[4] owing to their high porosity, thermal stability, structural diversity, and high compatibility.[5–7] The deposition of MOFs onto surfaces is of interest for these applications, and also for realizing optical devices.[8] The construction of surface-anchored MOFs (SURMOFs) through layer-by-layer liquid-phase epitaxy (LPE) is one approach for forming thin films and membranes for such applications.[9,10] In an LPE process, alternating deposition of inorganic and organic components onto the substrate allows fine control of the distribution and thickness of functional entities in thin films, by controlling the sequence and cycles of deposition.[11,12] Ideally, the growth mode of SURMOF thin films is expected to have a resolution of "one unit layer" and the thickness of the layers consisting of a specific component is proportional to the number of corresponding deposition cycles.[13] Indeed, using the SURMOF approach, the heteroepitaxial deposition of a variety of MOFs has been demonstrated[14] and the suppression of interpenetration of different components has been achieved.[15] This allows for thin-film structural flexibility,[16] and enabling applications, *e.g.*, in non-linear optics.[17,18]

With excellent crystalline order, the photophysical properties of SURMOFs make them potentially interesting materials for light harvesting, and photon emission.[19,20] Of particular interest in this context is the mobility of excitons, which affect the efficiency of the macroscopic transport properties.[21–24] Exciton diffusion is strongly dependent on the orientation of the chromophores and their distance. Thus, we are actively seeking to leverage the rich field of SURMOFs to produce well-defined, oriented thin films in which the positions of chromophores can be precisely controlled. In previous work, we fabricated a heterostructure with oriented 2D layers perpendicular to the substrate for triplet–triplet annihilation-based upconversion (TTA-UC).[25] The emission of TTA-UC requires efficient triplet motion in between sensitizer and emitter molecules, thus ensuring the collision of two triplets to form

[a] Institute of Microstructure Technology, Karlsruhe Institute of Technology, Hermann-von-Helmholtz-Platz 1, 76344 Eggenstein-Leopoldshafen, Germany. E-mail: tonghan.zhao@kit.edu, iahoward@gmail.com
[b] Institute of Solid State Physics, NAWI Graz, Graz University of Technology, Petersgasse 16, A-8010 Graz, Austria
[c] Light Technology Institute, Karlsruhe Institute of Technology, Engesserstrasse 13, 76131 Karlsruhe, Germany

† Electronic supplementary information (ESI) available. See DOI: https://doi.org/10.1039/d4tc00018h

‡ Present address: Carl Zeiss AG – Innovation Hub Karlsruhe, Hermann-von-Helmholtz-Platz 6, 76344 Eggenstein-Leopoldshafen, Germany.

one singlet exciton. The emission from this singlet excited state then has a higher energy than the incident photons (*i.e.*, upconversion). Unfortunately, the emission efficiency was suppressed in this 2D SURMOF because the fast axis of triplet motion parallel to substrate while the sensitizer and emitter 2D sheets perpendicular to the substrate.[24] To address this challenge, introducing a dinitrogen pillar linker to form layer pillar-type SURMOFs of the general formula M_2L_2P (M = metal ion, L = dicarboxylate, P = dinitrogen pillar ligand) would be an ideal strategy:[26] In this case the 2D-layer "sheets" can be separated by pillar linkers perpendicular to the substrate, therefore maximizing exciton transfer. To date, the vast majority of SURMOFs prepared with a desired [001] orientation (2D layers parallel to the substrate) are grown on gold substrates coated with organic thiol self-assembled monolayers (SAMs).[27,28] However, a much more ubiquitous substrate that meets these criteria is available – silicon (all the mentioned silicon substrates have a native oxide). Ott and coworkers reported [001]-oriented growth of $Cu_2(BDC)_2(DABCO)$, in which the 2D sheets of BDC parallel to the substrate and were separated by DABCO molecules, by only rinsing silicon with absolute ethanol before the step-by-step deposition of metal ions and linkers (BDC = 1,4-benzene dicarboxylic acid, DABCO = 1,4-diazabicyclo[2.2.2]octane).[29] However, Cu^{2+} ions typically exhibit a quenching effect on such luminescent materials.[30–32] Thus, it is desired to employ ions with a full-filled d orbital, such as Zn^{2+}, to retain the photoluminescence (PL) properties of the linkers.

Here, we first focus on developing a strategy for growing [001]-oriented $Zn_2(BDC)_2(DABCO)$ on an ethanol-rinsed Si⟨100⟩ substrate by the LPE method. Despite varying the synthesis conditions over a wide range, only poorly ordered Zn-type SURMOFs were obtained when directly growing them on the Si substrate. Considering stepwise LPE has demonstrated its ability to fabricate SURMOF heterostructures,[14,33] we explored the possibility of first growing a $Cu_2(BDC)_2(DABCO)$ SURMOF employing the established procedure,[29] on which – by heteroepitaxy – a series of $Zn_2(BDC)_2(DABCO)$ layers is deposited. These retained the highly-ordered [001] orientation of the $Cu_2(BDC)_2(DABCO)$ (Fig. 1). The $Zn_2(BDC)_2(DABCO)$ layers then serve as a spacer to separate the finally grown $Zn_2(ADC)_2(BPy)$ layers from the $Cu_2(BDC)_2(DABCO)$ SURMOF (ADC = 9,10-anthracenedicarboxylic acid, BPy = 4,4′-bipyridine). In this way, the luminescence quenching effect of Cu^{2+} is suppressed, while the blue-colored emission from the anthracene units contained in the ADC linkers is preserved.

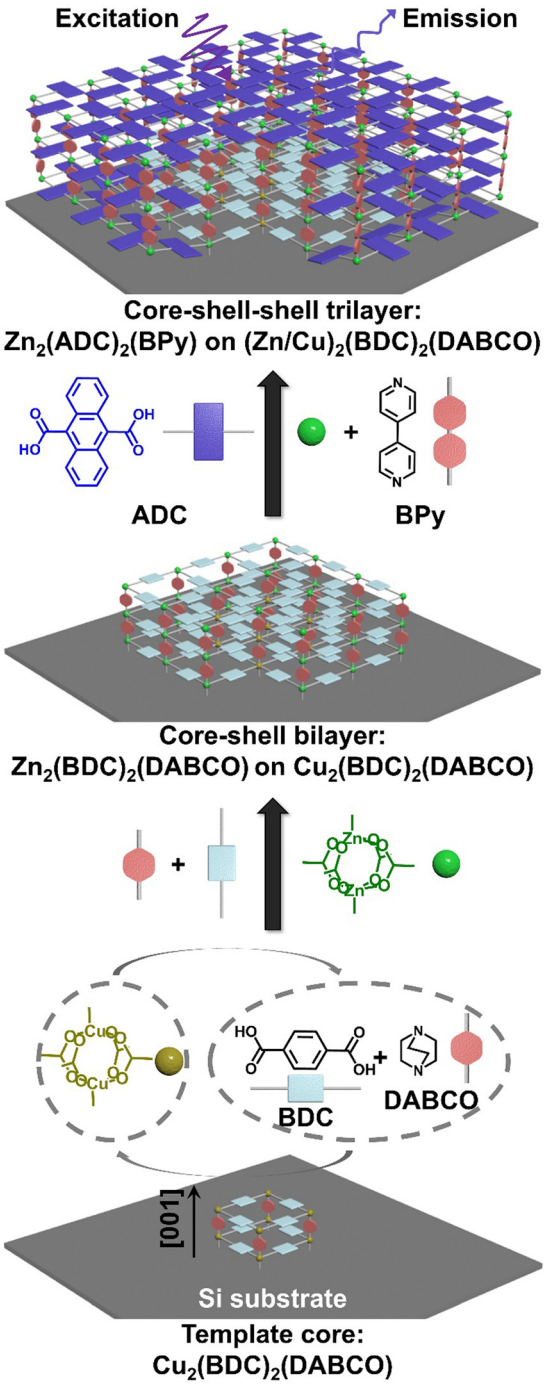

Fig. 1 Schematic illustration of the sequential deposition of SURMOF heterostructures. Additionally, the structure of the used components is shown. As a first step, a $Cu_2(BDC)_2(DABCO)$ SURMOF is prepared by alternating soaks of the substrate in an ethanol solution containing the copper ions and a solution containing a mixture of BDC/DABCO. In the second step, the copper is replaced with zinc, which results in the deposition of $Zn_2(BDC)_2(DABCO)$ on the originally grown $Cu_2(BDC)_2$-(DABCO) particles. This gives rise to the formation of core–shell $(Zn/Cu)_2$-$(BDC)_2(DABCO)$ heterostructure. Eventually, the growth of another emissive $Zn_2(ADC)_2(BPy)$ layer using ADC/BPy instead of BDC/DABCO leads to a core–shell–shell trilayer structure. In the schematics, a corner of the trilayer structure is removed to expose the core–shell and core–shell–shell thin film structures.

Results and discussion

Growth of [001]-oriented copper- and zinc-based pillar-layered SURMOFs

The SURMOFs were synthesized employing an automated pump setup, built according to the setup reported by McCarthy *et al.*[29] This system has the capability to immerse the substrate alternatively into solutions containing either the metal salt or linkers. As a starting point, we attempted the growth of

$Cu_2(BDC)_2(DABCO)$ using the protocol also from McCarthy *et al.*[29] The ⟨100⟩ polished Si wafer was rinsed with absolute ethanol three times and dried in a N_2 stream. The substrate was then transferred to the automated pump system substrate container (preheated to 60 °C) and soaked for 15 min in 1 mmol L^{-1} copper acetate ethanol solution, followed by rinsed twice with ethanol (for 0.5 and 4.5 min, respectively) except for the very first cycle of copper treatment, next soaked for 30 min in an ethanolic solution of 0.4 mmol L^{-1} BDC and 0.2 mmol L^{-1} DABCO, and rinsed twice with ethanol again (for 0.5 and 4.5 min, respectively). Then the cycle was repeated.

After 20 cycles, the formed SURMOF was investigated by out-of-plane X-ray diffraction (XRD), which confirmed the formation of a $Cu_2(BDC)_2(DABCO)$ structure on the ⟨100⟩ Si wafer (green line in Fig. 2a). The observation of several 2θ peaks (at 9.3°, 18.5°, and 27.8°) which can be associated with the (001) peaks, and of the otherwise strong (100) peak being suppressed, suggest a preferred orientation along the [001] direction. This result is consistent with the prior report.[29] Encouraged by these results, we repeated the fabrication replacing the Cu by a Zn salt. $Zn_2(BDC)_2(DABCO)$ SURMOF with 20 cycles was synthesized using the same procedure. In contrast, the out-of-plane XRD pattern of $Zn_2(BDC)_2(DABCO)$ exhibited both the (100) and (001) peaks at 8.3° and 9.2°, pointing toward a poor order. A texture equivalent to that in the $Cu_2(BDC)_2(DABCO)$ was not achieved.

To gain further insight into the degree of crystallite orientation across the substrate, we employed 2D grazing incidence wide-angle X-ray scattering (GIWAXS) to examine the $Cu_2(BDC)_2$-(DABCO) and $Zn_2(BDC)_2(DABCO)$ films. $Cu_2(BDC)_2(DABCO)$ crystallites result in unique points on the GIWAXS pattern (Fig. 2b), representing a very high degree of orientation, where the [001] direction is perpendicular to the substrate surface. On the contrary, the $Zn_2(BDC)_2(DABCO)$ sample GIWAXS pattern presents diffraction rings (Fig. 2c). One point to be noted is that the rings are more obvious on the (100) plane rather than on the (001) and (110) planes. This observation is interesting, and we envision a two-part possible explanation. The first is that a portion of the $Zn_2(BDC)_2(DABCO)$ grown along the (100) direction perpendicular to the substrate surface as we discussed above. However, the ring-shaped scattering pattern was mostly observed corresponding to the lattice parameters that originate from Zn coordinated with BDC only. Hence, we also considered the presence of impurities such as non-oriented Zn(BDC) as a second effect leading to the observed scattering pattern.[34,35] Scanning electronic spectroscopy (SEM) images of both $Cu_2(BDC)_2(DABCO)$ and $Zn_2(BDC)_2(DABCO)$ were taken to provide more evidence. As shown in Fig. 2d and e, SEM reveals dense island-shaped $Cu_2(BDC)_2(DABCO)$ crystallites on the surface. In contrast, $Zn_2(BDC)_2(DABCO)$ yielded surface with a poor homogeneity. Apart from parallel and perpendicularly aligned plates (regarded as [001]- and [100]-oriented crystals, respectively), a lot of small particles can be observed on the surface, which further confirms the formation of byproducts during the synthesis of $Zn_2(BDC)_2(DABCO)$. Attempts to optimize the orientation and phase purity of the samples by varying the preparation parameters, the concentration of the individual components in the precursor solutions, and the different substrates – for example, crystalline TiO_2- and Gd_2O_3-coated Si

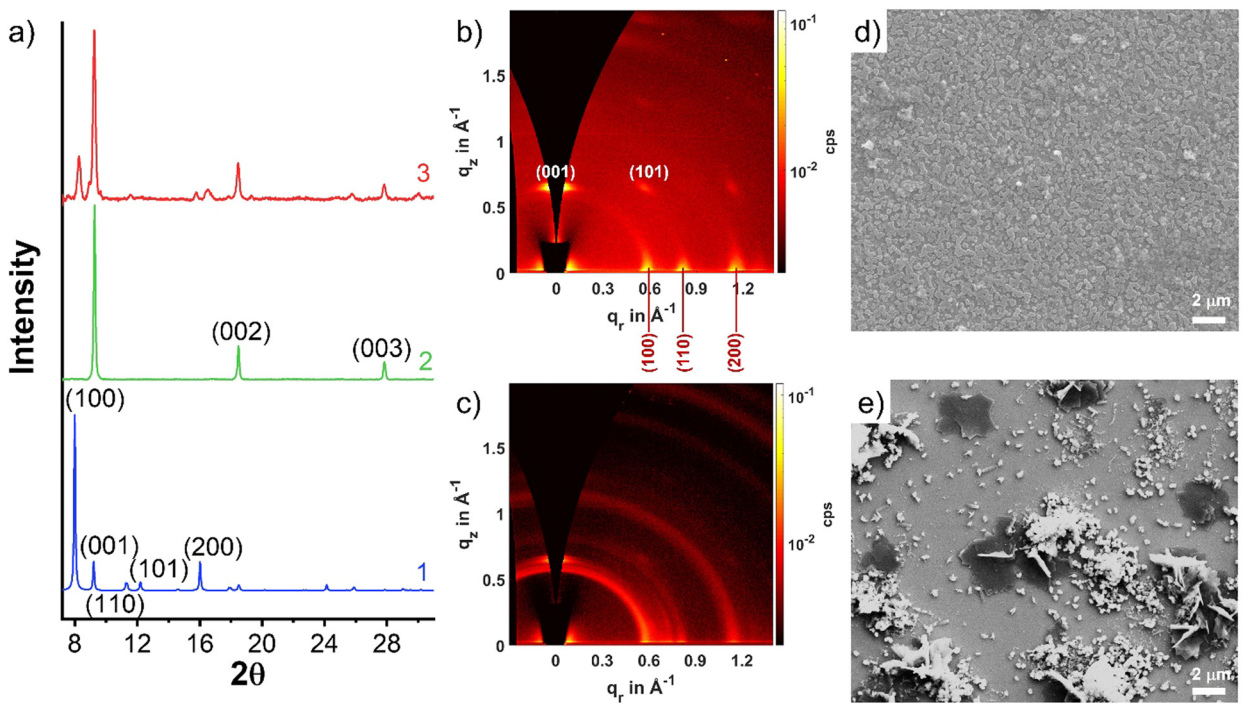

Fig. 2 (a) Experimental XRD patterns of $Cu_2(BDC)_2(DABCO)$ (2) and $Zn_2(BDC)_2(DABCO)$ (3) and simulated diffractogram for the DFT-optimized, fully activated structure of $Zn_2(BDC)_2(DABCO)$ (1) as 2 GIWAXS patterns of (b) $Cu_2(BDC)_2(DABCO)$ and (c) $Zn_2(BDC)_2(DABCO)$. SEM images of (d) $Cu_2(BDC)_2(DABCO)$ and (e) $Zn_2(BDC)_2(DABCO)$.

wafers as well as amorphous glass plate (Fig. S1, ESI†) – were not successful. These findings demonstrate that [001]-oriented $Zn_2(BDC)_2(DABCO)$ SURMOF is not well suited for a direct application of the LPE process on an ethanol-rinsed Si substrate.

Heteroepitaxial growth of [001]-oriented zinc-based pillar-layered SURMOFs on copper-based SURMOFs

The availability of high-quality $Cu_2(BDC)_2(DABCO)$ then made it possible to test whether heteroepitaxial growth of the Zn-based SURMOF is possible. As a first attempt, 18 cycles of $Zn_2(BDC)_2(DABCO)$ deposition were carried out after 2 cycles of $Cu_2(BDC)_2(DABCO)$ growth. This sample was named as 18C/2C-$(Zn/Cu)_2(BDC)_2(DABCO)$ and characterized by out-of-plane XRD, GIWAXS, and SEM. In addition, density functional theory (DFT) calculations were conducted on $Zn_2(BDC)_2(DABCO)$ for reference. The simulated lattice parameters for the tetragonal unit cell turned out to be $a = b = 11.05$ Å and $c = 9.59$ Å (Fig. 3a). Notably, these simulated values are quite consistent with the experimentally observed lattice parameters, which are $a = b = 10.92$ Å and $c = 9.61$ Å.[36] Specifically, parameters a and b showed a reduction of approximately 1.19%, while parameter c exhibited a slight increase of approximately 0.21%. As shown in Fig. 3b, the out-of-plane XRD of 18C/2C-$(Zn/Cu)_2(BDC)_2$-$(DABCO)$ has a good agreement with the simulated diffractogram of $Zn_2(BDC)_2(DABCO)$ with preferred orientation along the [001] direction, indicating 18C-$Zn_2(BDC)_2(DABCO)$ grew only in the [001] direction, perpendicular to the substrate surface on the 2C-$Cu_2(BDC)_2(DABCO)$ template. Regarding the GIWAXS pattern, the highly oriented growth of 18C/2C-$(Zn/Cu)_2(BDC)_2(DABCO)$ was demonstrated by the identical points at out-of-plane [001] and in-plane [100] directions as well as the diagonal (110) plane and off-axis (101) plane with almost no trace of scattering rings (Fig. 3c). By integrating the GIWAXS data along in-plane direction, we obtained the 1D GIWAXS in-plane diffraction pattern (Fig. 3d). This plot closely matches the simulated in-plane XRD pattern of $Zn_2(BDC)_2(DABCO)$. In addition, the SEM image in Fig. 3e reveals a plate-like morphology of 18C/2C-$(Zn/Cu)_2(BDC)_2(DABCO)$ with a width $\sim$1 μm. This agreement between experimental and simulated data validates the crystal structure of the material. In terms of a qualitative view of these results, the deposition of $Zn_2(BDC)_2$-$(DABCO)$ templated by $Cu_2(BDC)_2(DABCO)$ island seeds vastly improves the degree of preferential orientation of the $Zn_2(BDC)_2$-$(DABCO)$ – an extremely promising result.

For a quantitative analysis of orientation degree, we used the signal from the family {101} planes as a reporter. The scattering of this chosen peak does not position on $\vec{q}_z$ axis, so that we can extrapolate the intensity of the corresponding ring to the origin and measure the entire intensity of the peak by Gaussian fitting as we have done in previous work.[37] As the penetration depth of the X-rays is dependent on the incidence angle, α_i, of the primary beam in the GIWAXS technique, we collected a diffractogram for 18C/2C-$(Zn/Cu)_2(BDC)_2(DABCO)$ at $\alpha_i = 0.6°$ to obtain the scattering from the entire sample thickness (Fig. 4a). Afterwards, we prepared a pole figure (Fig. 4b), which is a commonly used approach for estimating the degree of orientational

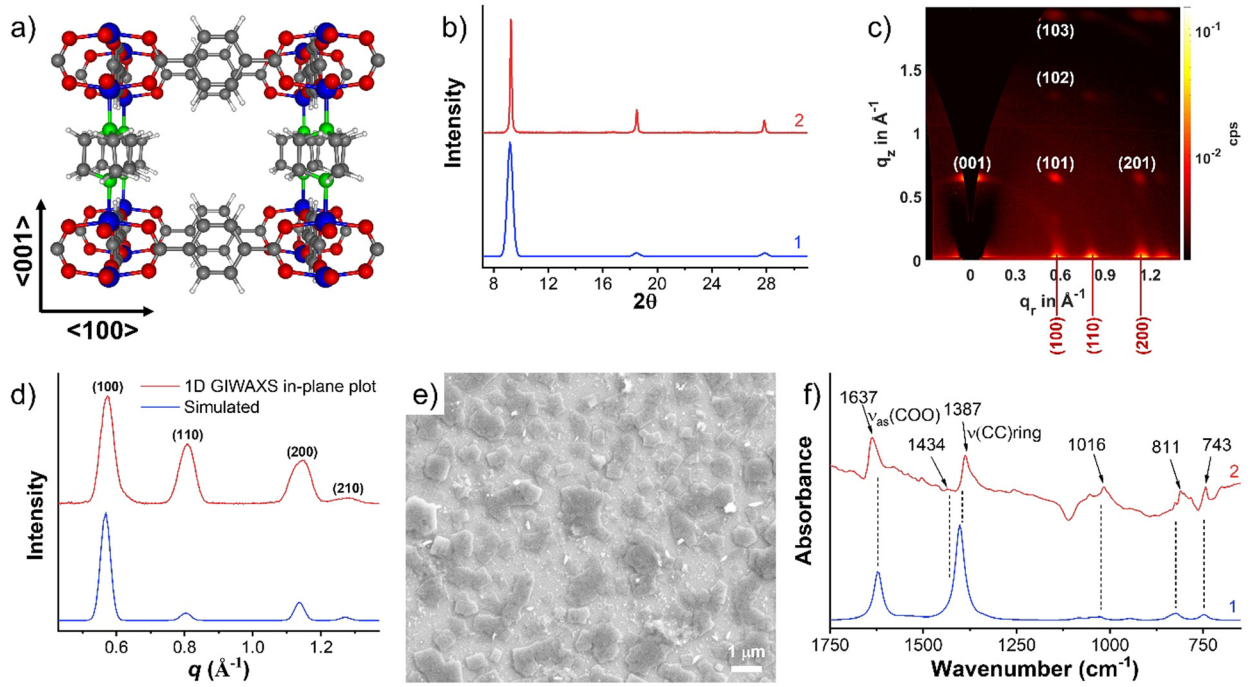

Fig. 3 (a) Simulated structure of $Zn_2(BDC)_2(DABCO)$ by DFT. Blue: Zn, gray: C, red: O, white: H. (b) Out-of-plane XRD pattern of 18C/2C-$(Zn/Cu)_2(BDC)_2(DABCO)$ (2) and simulated diffractogram of $Zn_2(BDC)_2(DABCO)$ with preferred orientation along the [001] direction (1) as reference. (c) 2D GIWAXS pattern of 18C/2C-$(Zn/Cu)_2(BDC)_2(DABCO)$. (d) Integrated 1D GIWAXS in-plane pattern of 18C/2C-$(Zn/Cu)_2(BDC)_2(DABCO)$ and simulated in-plane XRD pattern of $Zn_2(BDC)_2(DABCO)$ regarding the DFT calculation. (e) SEM image of 18C-$Zn_2(BDC)_2(DABCO)$ grows on 2C-$Cu_2(BDC)_2(DABCO)$. (f) FTIR-ATR spectra of experimental 18C/2C-$(Zn/Cu)_2(BDC)_2(DABCO)$ (2) and simulated $Zn_2(BDC)_2(DABCO)$ (1).

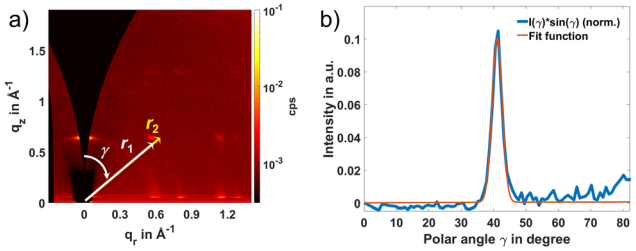

Fig. 4 (a) 2D GIWAXS pattern of 18C/2C-(Zn/Cu)$_2$(BDC)$_2$(DABCO) at 0.6° incidence angle. (b) sin(γ) corrected pole figure corresponding to data in (a) used to estimate that 93% of the film has a 2D powder texture.

order for a thin film based on GIWAXS.[38–40] To generate such a pole figure, the scattering intensity is integrated between a minimum and maximum cutoff radius, r_1 and r_2, then presented as a function of the angle to the $\vec{q}_z$ axis, γ. These angle and radii are illustrated in Fig. 4a. For the peak and ring that correspond to the scattering from the (101) peak of the 18C/2C-(Zn/Cu)$_2$(BDC)$_2$(DABCO), we take r_1 to be 0.82 and r_2 to be 0.90. To correct for nonsample-related scattering the background was taken at a slightly larger radius (r_1 = 0.96 and r_2 = 1.05) and subtracted from the measured signal. In addition, a correction to the pole figure to account for the fraction of the scattering signal observed at each γ was introduced.[37] This can be accomplished by multiplying the measured intensity, $I(\gamma)$, by sin(γ). The sin(γ) corrected pole figure so generated (shown in Fig. 4b), we can model with a Gaussian peak with almost no isotropic scattering in the background which indicates that scattering from a subset of the crystallites that have 2D powder texture with their [001] axis aligned to the surface normal clearly dominates. This procedure allows us to quantitatively conclude that ~93% of the scattering comes from the 2D powder texture so that the sample indeed has the desired high degree of surface orientation.

Considering those ideal results, we further deposited 3, 8, 13, 28, and 38 cycles of Zn$_2$(BDC)$_2$(DABCO) on top of 2 cycles of Cu$_2$(BDC)$_2$(DABCO). The XRD and GIWAXS patterns demonstrated a desired [001]-oriented growth of Zn$_2$(BDC)$_2$(DABCO) on 2C-Cu$_2$(BDC)$_2$(DABCO) with increasing cycles until 38 cycles (Fig. S2–S6, ESI†). 38C/2C-(Zn/Cu)$_2$(BDC)$_2$(DABCO) shows a scattering ring at the (100) plane which is similar to 20C-Zn$_2$(BDC)$_2$(DABCO). Fig. 6c and Fig. S6b (ESI†) compare GIWAXS measurements on 38C/2C-(Zn/Cu)$_2$(BDC)$_2$(DABCO) sample with different probing depths (α_i = 0.2° and 0.05° corresponding to a penetration depth of ~800 and ~6 nm in a smooth film, respectively). The 2D GIWAXS data shown here are similar for the two angles of incidence, suggesting the 38C/2C-(Zn/Cu)$_2$-(BDC)$_2$(DABCO) remains [001]-oriented across a large sample volume. In contrast, a thin film containing byproducts, as discussed earlier, shows (100), (200), and (300) scattering rings. The SEM image shows obvious cluster-like particles on the merging boundary of parallel aligned planes (Fig. S7, ESI†), confirming our hypothesis regarding scattering rings caused by impurities.

Identifying vibrational modes in the infrared absorption spectrum is a helpful step in confirming the chemical composition of a material. To achieve this, Fourier transform infrared spectroscopy with attenuated total reflection (FTIR-ATR) was employed to characterize 18C/2C-(Zn/Cu)$_2$(BDC)$_2$(DABCO). For comparison, the IR spectra for Zn$_2$(BDC)$_2$(DABCO) were also simulated and compared with the experimental results, as presented in Fig. 3f. The absorbance peak at 1637 cm^{-1} was assigned to the asymmetric carboxylate stretch, ν_{as}(COO), while the symmetric carboxylate stretching mode, ν_s(COO), was attributed to 1434 cm^{-1} peak. The separation of 203 cm^{-1} between these vibrational modes aligns well with established findings in the literature.[41] Furthermore, peaks at 1387 cm^{-1} correspond to the C=C vibrational modes of the benzene ring, while the peak at 1016 cm^{-1} is assigned to the phenyl vibrational C–H bending character. Additionally, peaks at 811 and 743 cm^{-1} correspond to the C–H rocking mode and hydrogen wagging modes in the BDC linker, respectively. These observed features, along with the peaks in the fingerprint region, closely match the simulated results (as shown in Fig. 3f). The good match between experimental and simulated data supports the conclusion that Zn$_2$(BDC)$_2$(DABCO) was successfully synthesized on top of Cu$_2$(BDC)$_2$(DABCO). Energy dispersive X-ray (EDX) analysis was conducted on the hetero (Zn/Cu)$_2$(BDC)$_2$-(DABCO) SURMOFs to gain insight into the elemental distribution with thin film depth. The EDX results indicate the content of Zn increases with the increasing deposition cycles in heterostructures as shown in Fig. S8a (ESI†). The elemental mapping of the cross section of the 38C/2C-(Zn/Cu)$_2$(BDC)$_2$(DABCO) film demonstrates a sufficient amount of Zn atoms (Fig. S8b–d, ESI†), further confirming the SURMOF grown with Zn.

To qualitatively estimate the thickness of (Zn/Cu)$_2$(BDC)$_2$-(DABCO) with a number of growth cycles of Zn-type MOF, we obtained high-resolution XRD data of the (001) peak of 2C-Cu$_2$(BDC)$_2$(DABCO) and Zn$_2$(BDC)$_2$(DABCO) with various deposition cycles on it (Fig. 5a). Subsequently, the full width at half maximum (FWHM) of the (001) XRD peaks were obtained by Gaussian fitting. The average thickness along [001] direction was estimated by Scherrer equation ($D_{(001)} = k\lambda/\beta\cos\theta$, where k is the Scherrer constant (0.89), λ is the wavelength of the X-ray (0.154 nm), β is the FWHM, θ is the Bragg angle of the peak). As show in Fig. 5b, the average height gradually increased with the number of growth cycles. The crystallite size demonstrates a

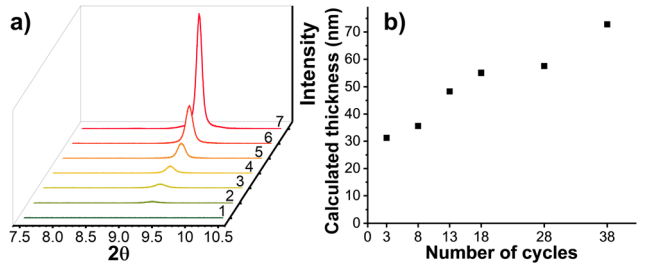

Fig. 5 (a) Out-of-plane XRD of 2C-Cu$_2$(BDC)$_2$(DABCO) (1), 3C/2C-(Zn/Cu)$_2$(BDC)$_2$(DABCO) (2), 8C/2C-(Zn/Cu)$_2$(BDC)$_2$(DABCO) (3), 13C/2C-(Zn/Cu)$_2$(BDC)$_2$(DABCO) (4), 18C/2C-(Zn/Cu)$_2$(BDC)$_2$(DABCO) (5), 28C/2C-(Zn/Cu)$_2$(BDC)$_2$(DABCO) (6), and 38C/2C-(Zn/Cu)$_2$(BDC)$_2$(DABCO) (7). (b) Calculated average thickness as a function of number of growth cycles.

nonlinear growth with respect to the number of cycles. This phenomenon has been reported also in the literature,[42,43] and may be attributed to a storage mechanism in which unreacted components are temporarily held on or in the already deposited SURMOF. The amount of precursor material accessible near the interface can then vary during each island growth step and thereby cause a nonlinearity in the development of crystallite size with the number of cycles. The estimated thickness of (38C/2C)-$(Zn/Cu)_2(BDC)_2(DABCO)$ is ~73 nm, agreeing well with the observed height in cross-sectional SEM image (Fig. S8b, ESI†). This observation indicates vertical growth of the SURMOF platelets. In addition, the gradual growth of the platelet width as the number of deposition cycles was increased from 3 to 38 can be retraced by SEM, until, finally, full coverage of the substrate is achieved (Fig. S7, ESI†). In other words, an island-type growth (Volmer–Weber growth) for the core–shell heterostructures was observed.[44,45] As illustrated in Fig. 6, the $Cu_2(BDC)_2(DABCO)$ first formed and distributed on the substrate in the shape of small islands. Then, alternating immersion between Zn and linkers solution produced $Zn_2(BDC)_2(DABCO)$ growing along both lateral and vertical directions on those islands. Further growth eventually leads to merging of individual islands, ultimately resulting in films that fully covered the substrate. It should be noted that the thin film resulting from this growth mode is not perfectly homogeneous, while Frank–Van der Merwe type growth should yield MOF films of nearly uniform thickness and without pinholes.[13,45–47] To improve the homogeneity, it may have something to do with the modification of substrates, selection of precursors, and conditions of synthesis. For instance, to facilitate MOF nucleation, the surface may require functionalization with active sites. This process usually involves the introduction of functional groups such as –COOH or the application of a metal oxide buffer layer, such as ZnO. Our laboratory is currently conducting further mechanistic studies and developing associated processes.

The $Cu_2(BDC)_2(DABCO)$-templated growth of pillar-layered Zn-type SURMOF with [001] orientation is not limited to the $Zn_2(BDC)_2(DABCO)$. $Zn_2(NDC)_2(DABCO)$ is a well-known MOF (NDC = naphthalene-1,4-dicarboxylic acid) that possesses similar lattice parameters to $Cu_2(BDC)_2(DABCO)$. Therefore, it serves as an initial target to synthesize a [001]-oriented SURMOF by using this heteroepitaxial method, following $Zn_2(BDC)_2(DABCO)$. Indeed, using 2C-$Cu_2(BDC)_2(DABCO)$ as a template, crystalline and highly [001]-oriented 20C-$Zn_2(NDC)_2$-(DABCO) could be obtained (XRD and GIWAXS patterns shown in Fig. S9, ESI†).

Core–shell–shell heterostructure

With a successful protocol established for growing well-oriented Zn-type SURMOF on $Cu_2(BDC)_2(DABCO)$, we next considered SURMOFs attractive for optical application, such as M_2L_2P-type MOFs that include photo- and electroactive ligands. These would be attractive for building functional materials by virtue of being able to tune two separate ligands. As detailed above, $Cu_2(BDC)_2(DABCO)$ is a useful template for developing controlled growth methodology, leaving one curious if a third layer oriented in [001] direction could be constructed on the core–shell $(Zn/Cu)_2(BDC)_2(DABCO)$ structure – particularly, if emissive linkers are involved in the third layer, the second shell $Zn_2(BDC)_2(DABCO)$ could serve as a spacer to prevent the fluorescence from quenching by copper (Fig. 7a). To verify this hypothesis, $Zn_2(ADC)_2(BPy)$ was a clear initial target. The ADC linker dissolved in ethanol can produce fluorescence at visible wavelengths and has an analogous transversal length to BDC. Choosing BPy as a pillar ligand could verify if the heteroepitaxial growth can happen in a SURMOF with lattice mismatch in the *c* parameter as well. BPy, thereby, should give new diffraction peaks at smaller angles which conveniently allows to distinguish the second shell from the underlying core–shell $(Zn/Cu)_2(BDC)_2(DABCO)$ structure.

We prepared 20C-$Zn_2(ADC)_2(BPy)$ grown on top of 3C/2C-$(Zn/Cu)_2(BDC)_2(DABCO)$ by the liquid-phase-epitaxy method. Examined by XRD leads to the observation of one single peak at 12.7° (q = 0.90 Å^{-1}) and a shoulder peak at 19.3° (q = 1.36 Å^{-1}). These two peaks correspond to the (004) and (006) planes along *c* axis, verified by comparison with the structural simulation of $Zn_2(ADC)_2(BPy)$ (Fig. S10a, ESI†). Although the first order (002) peak cannot be detected because of the instrument limitation, the integrated result of the out-of-plane GIWAXS pattern shows an obvious peak ~6.4° (q = 0.46 Å^{-1}), indicating the retention of the [001] orientation while deposited 20C-$Zn_2(ADC)_2(BPy)$ on 3C/2C-$(Zn/Cu)_2(BDC)_2(DABCO)$. As for the 2D GIWAXS pattern, several additional peaks were observed from this trilayer sample concerning 3C/2C-$(Zn/Cu)_2(BDC)_2(DABCO)$. Those (002), (004), and (112) peaks originating from $Zn_2(ADC)_2(BPy)$ indicates the preferential [001] orientation of 20C-$Zn_2(ADC)_2(BPy)$ (Fig. 7b). In addition, the out-of-plane integration plot of GIWAXS diffractograms with varying angles of incidence shows the intensity ratio of (004) of $Zn_2(ADC)_2(BPy)$ to (001) of $(Zn/Cu)_2(BDC)_2(DABCO)$ gradually increases with incidence angle decreasing, indicating the third layer is, in

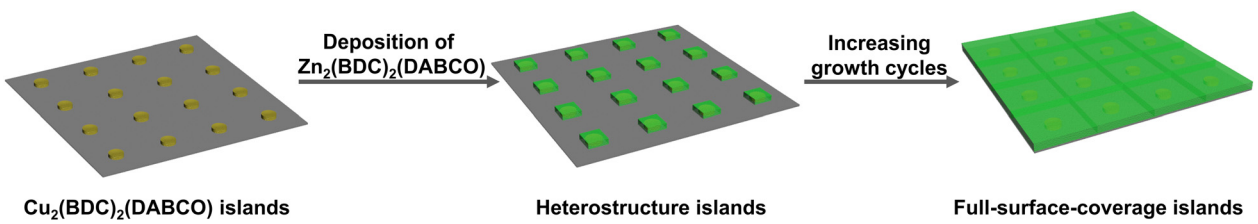

Fig. 6 Schematic showing layer-by-layer growth proceeds *via* the formation of islands and thus follows a Volmer–Weber-like growth mechanism.

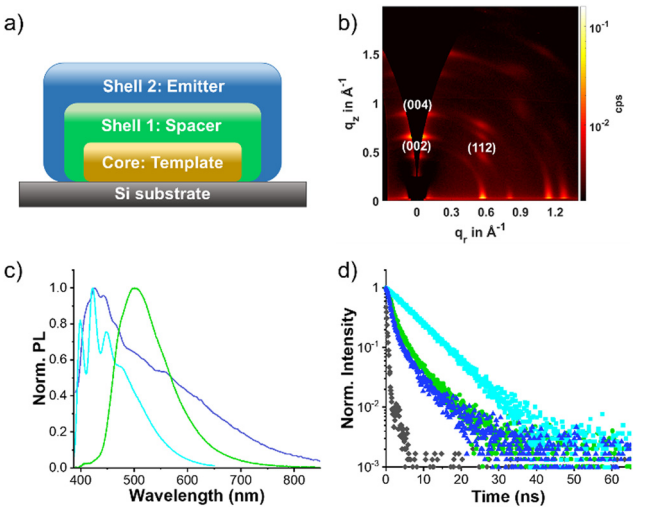

Fig. 7 (a) Illustration of core–shell–shell trilayer structure. (b) 2D GIWAXS patterns of $Zn_2(ADC)_2(BPy)$ grown on 3C/2C-$(Zn/Cu)_2(BDC)_2$(DABCO). (c) Normalized PL spectra of $Zn_2(ADC)_2(BPy)$ on 3C/2C-$(Zn/Cu)_2(BDC)_2$(DABCO) (blue line), ethanolic ADC solution (5×10^{-7} mol L^{-1}, cyan line), and drop-casted ADC film (green line). λ_{ex} = 300 nm. (d) Time-resolved PL decay of $Zn_2(ADC)_2(BPy)$ on 3C/2C-$(Zn/Cu)_2(BDC)_2$(DABCO) (blue triangle), ethanolic ADC solution (5×10^{-7} mol L^{-1}, cyan square) and drop-casted ADC film (green cycle) monitored at 426, 423, and 501 nm, respectively. λ_{ex} = 365 nm. Black square is the instrument response function of excitation source.

fact, on top of the core–shell structure (Fig. S10b, ESI†). This result further supports the successful fabrication of core–shell–shell structure.

Considering the second shell $Zn_2(BDC)_2$(DABCO) could keep $Zn_2(ADC)_2(BPy)$ from fluorescence quenching by Cu^{2+}, we carried out photophysical studies on this trilayer structure. For comparison, a drop-cast film of ADC from an ethanol solution on a Si substrate and a dilute ADC solution in ethanol at a concentration of 5×10^{-7} mol L^{-1} were also investigated. As shown in Fig. 7c, the steady-state fluorescence spectrum of the core–shell–shell $Zn_2(ADC)_2(BPy)$ on 3C/2C-$(Zn/Cu)_2(BDC)_2$(DABCO) exhibits a broad band with a maximum at 426 nm. ADC in ethanol shows three fine peaks at 399, 423, and 447 nm while the emission of ADC film centers at 501 nm. Additionally, time-resolved PL decay reveals a lifetime of the ADC solution emission of 7.11 ns, adopting a mono-exponential decay characteristic (Fig. 7d). However, analysis of the fluorescence decay of the core–shell–shell SURMOF at 426 nm reveals two emitting species with lifetimes of 1.23 and 6.45 ns, respectively. This pattern mirrors that of aggregated ADC films, which exhibit both short (2.15 ns) and long (6.33 ns) decay components (Table S1, ESI†). Within the $Zn_2(ADC)_2(BPy)$ lattice, ADC molecules are held apart vertically (along [001] direction) by BPy; yet they are proximal in the horizontal 2D sheet.[48] This arrangement allows for potential interactions between adjacent ADC or BPy molecules, which is also evident by the emission broadening. Despite the broad emission band, the lifetimes extracted from monitoring the PL decay at 426 and 501 nm are similar. Moreover, the decay tail bears resemblance to that of ADC molecules in ethanol. These observations suggest that ADC molecules within the SURMOF can engage in coupling states but also have the capability to emit as isolated monomers when excited.

Conclusions

In summary, we constructed a [001]-oriented core–shell–shell heretostructural SURMOF composed of $Cu_2(BDC)_2$(DABCO) core and $Zn_2(BDC)_2$(DABCO) and $Zn_2(ADC)_2(BPy)$ shells by the heteroepitaxial method. Using LPE, despite growing poorly oriented on its own, $Zn_2(BDC)_2$(DABCO) could be achieved in [001] orientation with a $Cu_2(BDC)_2$(DABCO) as an underlying oriented templated layer. This core–shell structure was systemically investigated and found to obey an island-type Volmer–Weber growth mechanism. In addition, a core–shell–shell SURMOF structure with the second shell $Zn_2(ADC)_2(BPy)$ serving as an emitter, the first shell $Zn_2(BDC)_2$(DABCO) as a spacer, and the core $Cu_2(BDC)_2$(DABCO) as the structural template was also achieved utilizing heteroepitaxy. Since $Zn_2(BDC)_2$(DABCO) could suppress the quenching effect of Cu^{2+}, the photoluminescence properties of $Zn_2(ADC)_2(BPy)$ could be examined. This study facilitates the fabrication of future designer optical materials with a common, single orientation.

Experimental

Materials

All reagents and solvents were used as received or otherwise indicated. Copper acetate monohydrate ($Cu(OOCCH_3)_2 \cdot H_2O$, 98%, Alfa Aesar), zinc acetate dihydrate ($Zn(OOCCH_3)_2 \cdot 2H_2O$, 97+%, Alfa Aesar), and 4,4′-bipyridine (BPy, 98%, Alfa Aesar) were purchased from ThermoFisher (Kandel) GmbH. Naphthalene-1,4-dicarboxylic acid (NDC, 99.66%) and 9,10-anthracenedicarboxylic acid (ADC, 98%) were purchased from BLD Pharmatech GmbH. 1,4-Bibenzene dicarboxylic acid (BDC) was purchased from Merck KGaA. 1,4-Diazabicyclo[2.2.2]octane (DABCO, ≥99%) was purchased from Sigma-Aldrich GmbH. Gd_2O_3@Si substrates with 150 nm Gd_2O_3 coated by molecular-beam epitaxy were purchased from Translucent Energy, Inc. Atomic layer deposition (ALD)-TiO_2-coated silicon substrates were prepared by using a Picosun R-series ALD reactor. The deposition was performed at 300 °C with 125 cycles. The pulsing and purging time for $TiCl_4$ was 0.1 s and 9 s, respectively; while water was 0.1 s and 13 s, respectively. The examined thickness of TiO_2 is 3 nm.

Characterization

2D grazing incidence wide angle X-ray scattering measurements were carried out on a Bruker D8 Advance equipped with a copper X-ray source (40 kV, 40 mA), Goebel mirror, a 0.5 mm micro mask and a 0.3 mm snout on the primary track and an Eiger 2R_500K detector on the secondary track. The reciprocal q-space GIWAXS scattering images was obtained with the GIXSGUI MATLAB plug-in.[49] X-ray diffraction patterns were obtained using a Bruker D2 Phaser diffractometer with CuKα radiation. The simulated XRD patterns of $Zn_2(NDC)_2$(DABCO)

and $Zn_2(ADC)_2(BPy)$ are based on single crystal .cif data in the literatures.[48,50] FTIR-ATR spectra were acquired on a Bruker VERTEX 70 FT-IR spectrometer. Steady-state photoluminescence was recorded with a Ocean Insight QE PRO spectrometer-based system using a UV LED (λ = 300 nm) as excitation source. Fluorescence decay was recorded on the Edinburgh Instruments FS5 spectrofluorometer with excitation by an external LED (365 nm). SEM images were taken on a ZEISS Supra 60VP. To examine the cross section image at the sample center, the sample was broken in half prior to measurement.

Synthesis of SURMOFs

The SURMOF synthesis on different substrates was performed, as previously reported, using the pump sequence by McCarthy *et al.*[29] Typically, for $Cu_2(BDC)_2(DABCO)$ the epitaxial growth process consists of alternately immersing a ⟨100⟩ Si substrate into an ethanolic solution of the building units: $Cu(OOCCH_3)_2{\cdot}H_2O$ (1 mmol L^{-1}, 15 min) and BDC/DABCO (0.4/0.2 mmol L^{-1}, 30 min). Between each soaking step, the substrates were rinsed thoroughly with ethanol for two times (0.5 and 4.5 min each). The temperature of the heating bath was fixed at 60 °C. The pump sequence lacked the ethanol-only immersion between the very first metal ion and ligand immersion. For zinc-type SURMOFs, ethanolic solution of $Zn(OOCCH_3)_2{\cdot}2H_2O$ (1 mmol L^{-1}) was used, and the concentration of BDC, NDC, ADC, DABCO, and BPy in ethanol were fixed at 0.2 mmol L^{-1}.

Simulation

We employed the Fritz Haber Institute (FHI-aims) code,[51] based on density functional theory (DFT), to investigate the stability and equilibrium structural parameters of $Zn_2(BDC)_2DABCO$. To determine the minimum energy structure, we initially utilized the Perdew–Burke–Ernzerhof (PBE) functional,[52] augmented with many-body dispersion correction.[53] We selected ''tight'' settings within FHI-aims and carried out computations with a well-converged 2 × 2 × 2 *k*-points grid, systematically sampling the Brillouin zone. Strict convergence criteria were enforced for variations in charge density (10^{-5}), total energy (10^{-6} eV), and forces (10^{-4} eV $Å^{-1}$) to ensure the highest precision. To determine Kohn–Sham eigenstate occupations, we applied a Gaussian broadening function with a σ = 0.01 eV width, significantly enhancing electronic state evaluations. Relativistic effects were accurately accounted for using the atomic Zeroth-Order Regular Approximation (ZORA).[54] In local geometry optimizations, an advanced iteration of the Broyden–Fletcher–Shanno–Goldfarb (BFGS) optimization algorithm,[51] incorporating the trust radius method, facilitated the identification of minima on the potential energy surface. Throughout the optimization process, convergence was rigorously maintained, with a tolerance threshold of 10^{-3} eV $Å^{-1}$ consistently upheld.

For the IR calculations, FHI_aims code with the PBE functional underestimate IR peak positions. Switching to the hybrid functional improve alignment with experimental peaks. For calculating the IR spectrum, we turned to the CRYSTAL23 code.[55] Within this code, crystalline orbitals are expressed as linear combinations of localized atomic orbitals of Gaussian type. We employed the hybrid B3LYP functional,[56,57] accounting for dispersion interactions *via* the D3 correction. The lattice parameters were obtained from FHI-aims calculations and the atomic positions relaxed before conducting vibrational calculations (B3LYP-D3 shows underestimation of lattice constants compared to experimental data). The accuracy of the Coulomb and exchange series was controlled by setting thresholds equal to 9, 9, 9, 9, 18.[58] Reciprocal space was discretized using a Monkhorst–Pack 4 × 4 × 4 grid in the irreducible part of the Brillouin zone. We maintained a self-consistency procedure accuracy of no less than 10^{-11} atomic units (1 a.u. = 27.21 eV) to ensure the precision of our results.

Conflicts of interest

There are no conflicts to declare.

Acknowledgements

The authors gratefully acknowledge the Helmholtz Association for funding through HEMF, and the MTET program (Materials and Technologies for the Energy Transition) – Topic 1 – Photovoltaics (38.01.05), and the recruitment initiative of B. S. R. We acknowledge support by the KIT-Publication Fund of the Karlsruhe Institute of Technology. T. Z. gratefully acknowledges the support of the Helmholtz-OCPC Postdoctoral Exchange Program (ZD202131) and the National Natural Science Foundation of China (22205045).

References

1 Y. J. Ma, X. Y. Fang, G. W. Xiao and D. P. Yan, Dynamic Manipulating Space -Resolved Persistent Luminescence in Core-Shell Mofs Heterostructures Via Reversible Photochromism, *Angew. Chem., Int. Ed.*, 2022, **61**, e202114100.
2 Y. Cui, H. Xu, Y. Yue, Z. Guo, J. Yu, Z. Chen, J. Gao, Y. Yang, G. Qian and B. Chen, A Luminescent Mixed-Lanthanide Metal–Organic Framework Thermometer, *J. Am. Chem. Soc.*, 2012, **134**, 3979–3982.
3 M. Tu, H. Reinsch, S. Rodríguez-Hermida, R. Verbeke, T. Stassin, W. Egger, M. Dickmann, B. Dieu, J. Hofkens, I. F. J. Vankelecom, N. Stock and R. Ameloot, Reversible Optical Writing and Data Storage in an Anthracene-Loaded Metal-Organic Framework, *Angew. Chem., Int. Ed.*, 2019, **58**, 2423–2427.
4 D. F. Sava Gallis, L. E. S. Rohwer, M. A. Rodriguez, M. C. Barnhart-Dailey, K. S. Butler, T. S. Luk, J. A. Timlin and K. W. Chapman, Multifunctional, Tunable Metal-Organic Framework Materials Platform for Bioimaging Applications, *ACS Appl. Mater. Interfaces*, 2017, **9**, 22268–22277.
5 Z. L. Zheng, N. Hanikel, H. Lyu and O. M. Yaghi, Broadly Tunable Atmospheric Water Harvesting in Multivariate Metal-Organic Frameworks, *J. Am. Chem. Soc.*, 2022, **144**, 22669–22675.

6 J. Zhang, Y. Shen, N. Jin, X. Zhao, H. Li, N. Ji, Y. Li, B. Zha, L. Li, X. Yao, S. Zhang, F. Huo and W. Zhang, Chemo-Biocascade Reactions Enabled by Metal–Organic Framework Micro-Nanoreactor, *Research*, 2022, **2022**, 9847698.

7 J. Wang, T. Feng, J. Chen, J.-H. He and X. Fang, Flexible 2d Cu Metal: Organic Framework@Mxene Film Electrode with Excellent Durability for Highly Selective Electrocatalytic Nh3 Synthesis, *Research*, 2022, 9837012.

8 H. Li, D. D. Liu, K. Khan, J. Shao, X. S. Liu, R. Cao, C. Y. Ma, F. L. Chong, A. K. Tareen, F. Hu, M. F. Mei, Y. Sun, D. X. Teng, S. Wageh, A. A. Al-Ghamdi, Z. Shi and H. Zhang, Two-Dimensional Metal Organic Frameworks for Photonic Applications [Invited], *Opt. Mater. Express*, 2022, **12**, 1102–1121.

9 J. X. Liu and C. Woll, Surface-Supported Metal-Organic Framework Thin Films: Fabrication Methods, Applications, and Challenges, *Chem. Soc. Rev.*, 2017, **46**, 5730–5770.

10 A. L. Semrau, Z. Y. Zhou, S. Mukherjee, M. Tu, W. J. Li and R. A. Fischer, Surface-Mounted Metal–Organic Frameworks: Past, Present, and Future Perspectives, *Langmuir*, 2021, **37**, 6847–6863.

11 O. Shekhah, H. Wang, S. Kowarik, F. Schreiber, M. Paulus, M. Tolan, C. Sternemann, F. Evers, D. Zacher, R. A. Fischer and C. Woll, Step-by-Step Route for the Synthesis of Metal-Organic Frameworks, *J. Am. Chem. Soc.*, 2007, **129**, 15118–15119.

12 K. Ikigaki, K. Okada and M. Takahashi, Epitaxial Growth of Multilayered Metal-Organic Framework Thin Films for Electronic and Photonic Applications, *ACS Appl. Nano Mater.*, 2021, **4**, 3467–3475.

13 S. Goswami, M. Rimoldi, R. Anderson, C. Lee, X. L. Li, A. Li, P. Deria, L. X. Chen, R. D. Schaller, D. A. Gomez-Gualdron, O. K. Farha and J. T. Hupp, Toward Ideal Metal-Organic Framework Thin-Film Growth Via Automated Layer-by-Layer Deposition: Examples Based on Perylene Diimide Linkers, *Chem. Mater.*, 2022, **34**, 9446–9454.

14 O. Shekhah, K. Hirai, H. Wang, H. Uehara, M. Kondo, S. Diring, D. Zacher, R. A. Fischer, O. Sakata, S. Kitagawa, S. Furukawa and C. Woll, Mof-on-Mof Heteroepitaxy: Perfectly Oriented [Zn-2(Ndc)(2)(Dabco)](N) Grown on [Cu-2(Ndc)(2)(Dabco)](N) Thin Films, *Dalton Trans.*, 2011, **40**, 4954–4958.

15 O. Shekhah, H. Wang, M. Paradinas, C. Ocal, B. Schupbach, A. Terfort, D. Zacher, R. A. Fischer and C. Woll, Controlling Interpenetration in Metal-Organic Frameworks by Liquid-Phase Epitaxy, *Nat. Mater.*, 2009, **8**, 481–484.

16 S. Wannapaiboon, A. Schneemann, I. Hante, M. Tu, K. Epp, A. L. Semrau, C. Sternemann, M. Paulus, S. J. Baxter, G. Kieslich and R. A. Fischer, Control of Structural Flexibility of Layered-Pillared Metal-Organic Frameworks Anchored at Surfaces, *Nat. Commun.*, 2019, **10**, 346.

17 C. Gu, H. Zhang, P. X. You, Q. Zhang, G. Q. Luo, Q. Shen, Z. B. Wang and J. B. Hu, Giant and Multistage Nonlinear Optical Response in Porphyrin-Based Surface-Supported Metal-Organic Framework Nanofilms, *Nano Lett.*, 2019, **19**, 9095–9101.

18 Y.-H. Xiao, Z.-Z. Ma, X.-X. Yang, D.-S. Li, Z.-G. Gu and J. Zhang, Inducing Circularly Polarized Luminescence by Confined Synthesis of Ultrasmall Chiral Carbon Nanodot Arrays in Pyrene-Based Mof Thin Film, *ACS Nano*, 2023, **17**, 19136–19143.

19 L. Y. Cao, Z. K. Lin, W. J. Shi, Z. Wang, C. K. Zhang, X. F. Hu, C. Wang and W. B. Lin, Exciton Migration and Amplified Quenching on Two-Dimensional Metal-Organic Layers, *J. Am. Chem. Soc.*, 2017, **139**, 7020–7029.

20 Y. B. Tian, K. Tanaka, L. M. Chang, C. Wöll, Z. G. Gu and J. Zhang, Highly Efficient Light Helicity Detection of Enantiomers by Chiral Metal-Organic Framework Thin Films, *Nano Lett.*, 2023, **23**, 5794–5801.

21 M. C. So, S. Jin, H. J. Son, G. P. Wiederrecht, O. K. Farha and J. T. Hupp, Layer-by-Layer Fabrication of Oriented Porous Thin Films Based on Porphyrin-Containing Metal-Organic Frameworks, *J. Am. Chem. Soc.*, 2013, **135**, 15698–15701.

22 R. Haldar, M. Jakoby, A. Mazel, Q. Zhang, A. Welle, T. Mohamed, P. Krolla, W. Wenzel, S. Diring, F. Odobel, B. S. Richards, I. A. Howard and C. Woll, Anisotropic Energy Transfer in Crystalline Chromophore Assemblies, *Nat. Commun.*, 2018, **9**, 4332.

23 C. Gu, H. Zhang, J. H. Yu, Q. Shen, G. Q. Luo, X. Chen, P. Xue, Z. B. Wang and J. B. Hu, Assembled Exciton Dynamics in Porphyrin Metal-Organic Framework Nanofilms, *Nano Lett.*, 2021, **21**, 1102–1107.

24 M. Adams, M. Kozlowska, N. Baroni, M. Oldenburg, R. Ma, D. Busko, A. Turshatov, G. Emandi, M. O. Senge, R. Haldar, C. Woll, G. U. Nienhaus, B. S. Richards and I. A. Howard, Highly Efficient One-Dimensional Triplet Exciton Transport in a Palladium-Porphyrin-Based Surface-Anchored Metal-Organic Framework, *ACS Appl. Mater. Interfaces*, 2019, **11**, 15688–15697.

25 M. Oldenburg, A. Turshatov, D. Busko, S. Wollgarten, M. Adams, N. Baroni, A. Welle, E. Redel, C. Woll, B. S. Richards and I. A. Howard, Photon Upconversion at Crystalline Organic-Organic Heterojunctions, *Adv. Mater.*, 2016, **28**, 8477–8482.

26 F. ZareKarizi, M. Joharian and A. Morsali, Pillar-Layered Mofs: Functionality, Interpenetration, Flexibility and Applications, *J. Mater. Chem. A*, 2018, **6**, 19288–19329.

27 A. Betard and R. A. Fischer, Metal-Organic Framework Thin Films: From Fundamentals to Applications, *Chem. Rev.*, 2012, **112**, 1055–1083.

28 J. L. Zhuang, A. Terfort and C. Woll, Formation of Oriented and Patterned Films of Metal-Organic Frameworks by Liquid Phase Epitaxy: A Review, *Coord. Chem. Rev.*, 2016, **307**, 391–424.

29 B. D. McCarthy, T. Liseev, A. M. Beiler, K. L. Materna and S. Ott, Facile Orientational Control of M2l2p Surmofs on < 100 > Silicon Substrates and Growth Mechanism Insights for Defective Mofs, *ACS Appl. Mater. Interfaces*, 2019, **11**, 38294–38302.

30 S. Sahu, S. Bishi and P. K. Behera, Fluorescence Quenching of 1-and 2-Naphthols by Cu2+ in Anionic Micelle, *J. Mol. Liq.*, 2011, **158**, 38–42.

31 M. Panda and K. Kabir-ud-Din, Fluorescence Quenching of Naphthols by Cu2+ in Micelles, *Arab. J. Chem.*, 2014, **7**, 261–266.
32 K. Szyszka, S. Targonska, A. Lewinska, A. Watras and R. J. Wiglusz, Quenching of the Eu^{3+} Luminescence by Cu^{2+} Ions in the Nanosized Hydroxyapatite Designed for Future Bio-Detection, *Nanomaterials*, 2021, **11**, 464.
33 B. Liu, M. Tu, D. Zacher and R. A. Fischer, Multi Variant Surface Mounted Metal-Organic Frameworks, *Adv. Funct. Mater.*, 2013, **23**, 3790–3798.
34 J. X. Liu, B. Lukose, O. Shekhah, H. K. Arslan, P. Weidler, H. Gliemann, S. Brase, S. Grosjean, A. Godt, X. L. Feng, K. Mullen, I. B. Magdau, T. Heine and C. Woll, A Novel Series of Isoreticular Metal Organic Frameworks: Realizing Metastable Structures by Liquid Phase Epitaxy, *Sci. Rep.*, 2012, **2**, 921.
35 Z. Wang, K. Rodewald, R. Medishetty, B. Rieger and R. A. Fischer, Control of Water Content for Enhancing the Quality of Copper Paddle-Wheel-Based Metal Organic Framework Thin Films Grown by Layer-by-Layer Liquid-Phase Epitaxy, *Cryst. Growth Des.*, 2018, **18**, 7451–7459.
36 D. N. Dybtsev, H. Chun and K. Kim, Rigid and Flexible: A Highly Porous Metal-Organic Framework with Unusual Guest-Dependent Dynamic Behavior, *Angew. Chem., Int. Ed.*, 2004, **43**, 5033–5036.
37 J. C. Fischer, C. Li, S. Hamer, L. Heinke, R. Herges, B. S. Richards and I. A. Howard, Giwaxs Characterization of Metal-Organic Framework Thin Films and Heterostructures: Quantifying Structure and Orientation, *Adv. Mater. Interfaces*, 2023, **10**, 2202259.
38 M. R. Hammond, R. J. Kline, A. A. Herzing, L. J. Richter, D. S. Germack, H. W. Ro, C. L. Soles, D. A. Fischer, T. Xu, L. P. Yu, M. F. Toney and D. M. DeLongchamp, Molecular Order in High-Efficiency Polymer/Fullerene Bulk Heterojunction Solar Cells, *ACS Nano*, 2011, **5**, 8248–8257.
39 J. Rivnay, S. C. B. Mannsfeld, C. E. Miller, A. Salleo and M. F. Toney, Quantitative Determination of Organic Semiconductor Microstructure from the Molecular to Device Scale, *Chem. Rev.*, 2012, **112**, 5488–5519.
40 A. Mahmood and J. L. Wang, A Review of Grazing Incidence Small- and Wide-Angle X-Ray Scattering Techniques for Exploring the Film Morphology of Organic Solar Cells, *Sol. RRL*, 2020, **4**, 2000337.
41 K. Tan, N. Nijem, P. Canepa, Q. Gong, J. Li, T. Thonhauser and Y. J. Chabal, Stability and Hydrolyzation of Metal Organic Frameworks with Paddle-Wheel Sbus Upon Hydration, *Chem. Mater.*, 2012, **24**, 3153–3167.
42 H. K. Arslan, O. Shekhah, J. Wohlgemuth, M. Franzreb, R. A. Fischer and C. Wöll, High-Throughput Fabrication of Uniform and Homogenous Mof Coatings, *Adv. Funct. Mater.*, 2011, **21**, 4228–4231.
43 K. Yusenko, M. Meilikhov, D. Zacher, F. Wieland, C. Sternemann, X. Stammer, T. Ladnorg, C. Wöll and R. A. Fischer, Step-by-Step Growth of Highly Oriented and Continuous Seeding Layers of $[Cu_2(Ndc)_2(Dabco)]$ on Bare Oxide and Nitride Substrates, *CrystEngComm*, 2010, **12**, 2086–2090.
44 A. Summerfield, I. Cebula, M. Schroder and P. H. Beton, Nucleation and Early Stages of Layer-by-Layer Growth of Metal Organic Frameworks on Surfaces, *J. Phys. Chem. C*, 2015, **119**, 23544–23551.
45 M. L. Ohnsorg, C. K. Beaudoin and M. E. Anderson, Fundamentals of Mof Thin Film Growth Via Liquid-Phase Epitaxy: Investigating the Initiation of Deposition and the Influence of Temperature, *Langmuir*, 2015, **31**, 6114–6121.
46 D.-H. Chen, H. Gliemann and C. Wöll, Layer-by-Layer Assembly of Metal-Organic Framework Thin Films: Fabrication and Advanced Applications, *Chem. Phys. Rev.*, 2023, **4**, 011305.
47 O. Lugier, U. Pokharel and S. Castellanos, Impact of Synthetic Conditions on the Morphology and Crystallinity of Fdmof-1(Cu) Thin Films, *Cryst. Growth Des.*, 2020, **20**, 5302–5309.
48 Q. Gao, Y. B. Xie, J. R. Li, D. Q. Yuan, A. A. Yakovenko, J. H. Sun and H. C. Zhou, Tuning the Formations of Metal-Organic Frameworks by Modification of Ratio of Reactant, Acidity of Reaction System, and Use of a Secondary Ligand, *Cryst. Growth Des.*, 2012, **12**, 281–288.
49 Z. Jiang, GIXSGUI: a MATLAB toolbox for grazing-incidence X-ray scattering data visualization and reduction, and indexing of buried three-dimensional periodic nanostructured films, *J. Appl. Crystallogr.*, 2015, **48**, 917–926.
50 H. Chun, D. N. Dybtsev, H. Kim and K. Kim, Synthesis, X-Ray Crystal Structures, and Gas Sorption Properties of Pillared Square Grid Nets Based on Paddle-Wheel Motifs: Implications for Hydrogen Storage in Porous Materials, *Chem. – Eur. J.*, 2005, **11**, 3521–3529.
51 V. Blum, R. Gehrke, F. Hanke, P. Havu, V. Havu, X. G. Ren, K. Reuter and M. Scheffler, Molecular Simulations with Numeric Atom-Centered Orbitals, *Comput. Phys. Commun.*, 2009, **180**, 2175–2196.
52 J. P. Perdew, K. Burke and M. Ernzerhof, Generalized Gradient Approximation Made Simple, *Phys. Rev. Lett.*, 1996, **77**, 3865–3868.
53 A. Tkatchenko, R. A. DiStasio, R. Car and M. Scheffler, Accurate and Efficient Method for Many-Body van der Waals Interactions, *Phys. Rev. Lett.*, 2012, **108**, 236402.
54 E. v Lenthe, E. J. Baerends and J. G. Snijders, Relativistic Regular Two-Component Hamiltonians, *J. Chem. Phys.*, 1993, **99**, 4597–4610.
55 A. Erba, J. K. Desmarais, S. Casassa, B. Civalleri, L. Donà, I. J. Bush, B. Searle, L. Maschio, L. Edith-Daga, A. Cossard, C. Ribaldone, E. Ascrizzi, N. L. Marana, J. P. Flament and B. Kirtman, Crystal23: A Program for Computational Solid State Physics and Chemistry, *J. Chem. Theory Comput.*, 2023, **19**, 6891–6932.
56 C. T. Lee, W. T. Yang and R. G. Parr, Development of the Colle-Salvetti Correlation-Energy Formula into a Functional of the Electron-Density, *Phys. Rev. B*, 1988, **37**, 785–789.
57 A. D. Becke, Density-Functional Thermochemistry. III. The Role of Exact Exchange, *J. Chem. Phys.*, 1993, **98**, 5648–5652.
58 A. Erba, M. Rérat, S. Casassa, B. Searle, J. Desmarais, D. de Quımica Fısica, R. Dovesi, V. R. Saunders, C. Roetti, R. Orlando, C. M. Zicovich-Wilson, F. Pascale, B. Civalleri, K. Doll, N. M. Harrison, I. J. Bush, P. H. D'arco, M. Llunell, M. Causa, Y. Noël and L. Maschio, Users' Maual of Crystal23, 2022.